Chapter 04

An improved dislocation density reliant model to address the creep deformation of reduced activation ferritic martensitic steel

Abstract: The blanket module of nuclear fusion reactor is proposed to be made of reduced activation ferritic martensitic (RAFM) steel. Thus, in order to prevent the unprecedented failure, the creep response of RAFM steel must be studied meticulously. In that direction, physical based creep curve modelling is one of the available choices to obtain the insights about the substructural evolution during the creep deformation, hence enabling to enlighten about material weakening mechanisms. In this chapter, experimental creep curves of RAFM steel at varying conditions are simulated employing an improved dislocation density reliant physical model. The microstructure based internal variables are considered for addressing the mechanisms such as hardening, recovery, coarsening of precipitates and creep cavitation. All the simulated creep curves are found to be in reasonable agreement with the experimental creep curves. The predicted values of the different variables such as dislocation glide velocity, climb velocity, internal stress, climb stress, effective stress, mobile dislocation density, dipole dislocation density, boundary dislocation density, subgrain radius, boundary pressure, boundary dislocation spacing, subgrain mobility and dipole capture spacing. Furthermore, the evolution of involved eighteen parameters is demonstrated and discussed thoroughly.

4.1. Introduction

The construction of the international thermonuclear experimental reactor was aimed at the proliferation of the technology of fusion energy for future electricity demand. The first wall and blanket module is found to be an important shield among all the fusion reactors components and

it is proposed to be made of RAFM steel [9, 13, 141-148]. This steel is found to be cheaper, exhibit excellent resistance against high energy neutron irradiation [146] and possess decent high-temperature mechanical properties, hence suitable for the aforementioned applications [9, 13, 146, 149, 150]. The constituents inside the microstructure of RAFM steel are similar to that of 9-12 % Cr steels and includes a high number of dislocation population as well as numerous types of interfaces (prior austenitic grain boundary, block boundary, packet boundary and lath boundary) decorated with $(Cr, Fe)_{23}C_6$ carbides ($M_{23}C_6$-type). Further, V and Ta based carbo-nitrides (MX-type) are distributed inside the matrix as well as at the subgrain boundaries and all together makes the RAFM, a good creep resistance material [13, 14, 57, 58, 141, 144]. The service conditions of RAFM steel components can be varied over a wide range of temperature and stresses, i.e., 500-600 ^{o}C and 100-300 MPa, respectively [150]. In that severe conditions, this steel is susceptible to the microstructural degradation during the exposure period and out of many, creep mechanism is one of the responsible factor for the weakening of the material. Thus, anatomy of the induced microstructure with ongoing creep will play a crucial role in the safe life estimation of components and for the new alloys development programs. Modelling and simulation can be a proficient alternative technique to the analytical solutions that need as the progress of time[151]. In this direction, dislocation density based physical modelling is a decent choice, as it elucidates the complex deformation behaviours as well as provides the insights about the ongoing substructure evolution. For example, in case of fixed strain rate deformation tests, the physical based models have been developed by many researchers[3, 27, 41, 63, 152] to capture the microstructural development with ongoing strain/deformation. Barlat et al. [27] proposed the dislocation reliant physical model that considers mobile dislocation density, forest dislocation density and mean free path as internal variables to address the constant strain rate deformation of aluminum alloys. The

approach was further explored by Surya et al. [41] to address the deformation and ongoing substructural evolution in a 304 HCu steel. Over the years, Lindgren's group has proposed basic as well as advanced dislocation reliant physical models [3, 37, 63] that address the deformation behavior of AISI 316 L, Ti-6Al-4V and Inconel 718. Further, Xiao et al. [153] proposed the physical based constitutive model to study the deformation response in Ni_3Al-based superalloy. Similarly, in the recent past, number of physical-based creep models were also developed and their contribution is significant in understanding the creep response. The model developed by Ghoniem et al. [47] was utilized for addressing the creep behavior of HT-9 martensitic stainless steel and strain rate was considered to be the function of numerous variables as,

$$\dot{\varepsilon} = f\left(\rho_m, \rho_b, \rho_s, R_{sub}, T, \sigma_{app}, N_v, r_m\right), \tag{4.1}$$

In this work, analysis of the primary and secondary creep curve regime is nicely elucidated with the help of Orowan equation to estimate creep rate. Nonetheless, the tertiary creep curve regime is not analyzed due to complex phenomena in this regime. In the same direction, Blum et al. [154] proposed the creep model that considers the microstructure based variables such as single dislocation density, dipole dislocation density and the dislocation spacing. The model was validated for Al, Al-5 at. % Mg and Ti-6Al-4V alloys and the primary and secondary creep regimes were addressed nicely. In order to distinguish the heterogeneous dislocation substructure, Barkar et al.[155] proposed a composite model, coupled with precipitation kinetics and it was assumed that strain is equal in hard subgrain walls and soft subgrain interior regime. In this approach, free dislocation density, subgrain size, width of subgrain boundaries and free dislocation spacing were considered as important internal variables. The model dealt with the primary and secondary creep regime and validated with 9-12 % Cr steels. Furthermore, Magnusson et al. [49] developed a model to simulate the creep response for up to the secondary stage of 9-12% Cr steels, considering

the microstructure based variables such as free dislocation density, immobile dislocation density and subgrain size. Kai Song et al. [156] developed the model for Sanicro 25, which is based on the microstructure evolution and hardening mechanism.

In continuation with aforementioned physical-based creep models, it has to be mentioned that, empirical and hybrid models have been also developed to model the creep behavior of metallic materials. With respect to empirical models, McLean et al. [43] used the continuum damage mechanics (CDM) approach to address the primary and tertiary creep regime of a 12 % Cr steel. Similarly, Semba et al. [51] proposed the CDM based model that incorporates the damage evolution based on the Ostwald ripening, solid solution depletion and subgrain coarsening in order to address the creep curves of 9 % Cr steels. The approach was further developed by Oruganti et al. [157] by incorporating the temperature dependent subgrain coarsening and invoking the back stress concept. Considering the coarsening of carbides and carbonitrides, Murchu`et al. [59] developed a model to simulate the creep curves of 9 % Cr steel. In this model, hyperbolic sine function that incorporates various state variables was used to evaluate the creep rate. Despite, the model addressed the primary, secondary and tertiary creep regime nicely, for the stress range of 70-125 MPa, the evolution of dislocations substructure was not emphasized, which has an important role in creep phenomena. Further, Aktaa et al. [8] developed a coupled viscoelastic deformation damage model to study the constitutive behavior of RAFM steel with ongoing creep and fatigue, considering irradiation induced hardening and corresponding damage. This model explains the creep deformation of RAFM steel under creep-fatigue loading as well as at the high dose of irradiation conditions. It is observed that, at higher strain, the model shows negative influence of irradiation on the fatigue life time. Similarly, in an another work, creep curves of RAFM steel were modelled with the help of theta projection methodology by employing the

artificial neural network [14] to address the primary and tertiary creep regimes. Furthermore, Christopher et al. [66] used a constitutive model to simulate the creep curve of P91 steel, considering the damage due to dislocation density, solute depletion from the matrix and cavitation. This model is modified version of Dyson-McLean[43] approach and it was discussed that formation of Z-phase at the expense of carbonitride precipitates strongly influences the tertiary creep regime.

In context to hybrid approach, Basirat et al. [55] proposed a model to study the creep deformation behavior of nine percent chromium steel and creep rate is assimilated with the parameters as,

$$\dot{\varepsilon} = f\left(\rho_m\ , \rho_{dip}\ , \sigma_{app}, T, D_{cav}, D_{sol}, D_{ppt}\right), \tag{4.2}$$

This model can disseminate the creep curve up to the onset of tertiary regime. In continuation with aforementioned hybrid model, Surya et al. [57, 58, 158] developed the models for 9 % Cr steels to elucidate the creep deformation behavior and associated substructure evolution. Model relies on the microstructure based internal state variables to estimate the creep rate as,

$$\dot{\varepsilon} = f\left(\rho_m, \rho_b, \rho_{dip}, R_{sub}, T, \sigma_{app}, N_v, r_m, D_{cav}, D_{ppt}\right), \tag{4.3}$$

Following the model in [58], Florian et al. [159] proposed a model to investigate the creep curves and time-to-rupture diagram of P91 steel, considering the mobile dislocation density, static dislocation density, boundary dislocation, subgrain size, damage due to coarsening of precipitates and cavitation.

It is apparent from the above discussion that, the primary and secondary creep regimes have been studied nicely by some of the developed models [47-49, 154, 155]. Also, few of the recently developed models are capable to address the complete creep curves including tertiary creep regime [43, 51, 55, 57-59, 66, 157, 160]. *The problem lies in a way that, if models address complete creep curve then microstructural evolution and all other important parameters are not demonstrated*

[14, 43, 66]. *Similarly, if microstructural evolution is discussed, the models are not capable to address complete creep curves* [47, 49, 154, 156]. However, few parameters were captured and discussed in some of the recent works[51, 57-59, 157]. Impact of all internal variables during the creep exposure is very important and rarely reported, yet to be discussed for RAFM steel.

This chapter embodied an improved dislocation density based creep model (a physical based model in combination with CDM approach) for RAFM steel, built on the ground of Ghoniem et al.[47], Basirat et al.[55], and Surya et al. [58] work. The model demonstrates the capability to analyze the creep curves for up to the onset of tertiary regime. Involved internal variables and their evolution during the creep exposure is discussed thoroughly. Variation in the mobile dislocation density, dipole dislocation density, glide velocity, climb velocity, boundary dislocation spacing h_b, boundary pressure P_{sb}, subgrain boundary mobility M_{sb}, dipole capture spacing, internal stress, effective stress, climb stress, mean radius of MX (V and Ta based carbonitrides) precipitates, mean radius of $M_{23}C_6$ carbides, softening due to MX precipitates, softening due to $M_{23}C_6$ carbides and cavitation softening D_{cav} is addressed and demonstrated with the ongoing creep.

4.2. Material and methods

In this research work, for the modelling and validation purpose, the creep curves of RAFM steel at different stress and temperature, i.e., 280 MPa / 500 ℃, 140 MPa / 600 ℃, 200 MPa / 550 ℃ and 120 MPa / 600 ℃ were taken from literature [14, 161, 162]. The chemical composition of RAFM steel in [14] is given (in wt. %) as, Cr-9.04, W-1, V-0.22, C-0.08, Ta-0.06, N-0.0226, Nb-0.001, Mo-0.001, P, S-0.002, and Fe-rest. The steel underwent to normalizing and tempering heat treatment in order to have the tempered martensitic microstructure. The numerical simulation was carried out through MATLAB software employing ODE-45 solver. The simulated creep curves were compared with the experimental creep data for validation purpose. Input parameters like

initial dislocation density, subgrain radius, radius of precipitates and number density of precipitates were taken from literature and depicted in Table 4.1. Other model parameters and material constants utilized in this work are given in Appendix 4.A.

Table 4.1. Input parameters for simulation

Parameter	Value	Refs.
Mobile dislocation density (m^{-2})	4.00×10^{14}	[57, 58, 161]
Dipole dislocation density (m^{-2})	1.00×10^{14}	[57, 58]
Boundary dislocation density (m^{-2})	3.50×10^{14}	[57, 58]
Subgrain radius (m)	2.23×10^{-7}	[57, 58, 162, 163]
$M_{23}C_6$ precipitate radius (m)	55.00×10^{-9}	[10]
MX precipitate radius (m)	12.00×10^{-9}	[10]
Number density of $M_{23}C_6$ precipitate (m^{-3})	1.02×10^{18}	[10]
Number density of MX precipitate (m^{-3})	1.76×10^{20}	[10]

4.3. Model formulation

4.3.1. Representation of the microstructure

RAFM steel is made from certain alterations of radioactive elements in 9 % Cr steel that are replacement of Mo by W and Nb by Ta.

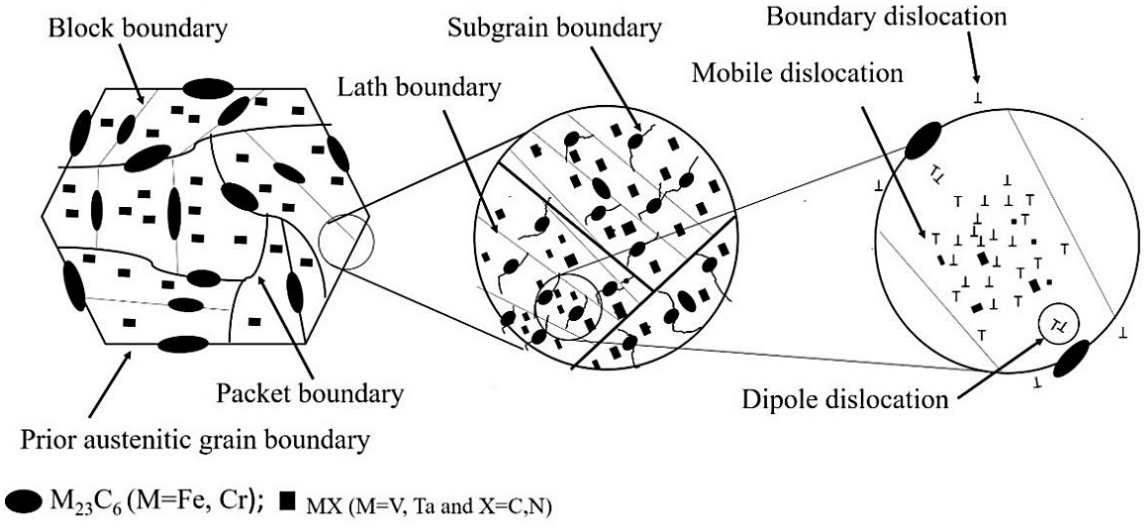

Figure 4.1. Schematic diagram of the representative microstructure of as-received tempered RAFM steel

It's a member of 9-12 % Cr steels that consists of tempered martensitic microstructure embodied with high dislocation density (Mobile, dipole and boundary), numerous interfaces (prior austenitic grain boundary, packet boundary, block boundary, lath boundary and subgrain boundary), $M_{23}C_6$ carbides and MX carbonitrides. The representative microstructure of as-received tempered RAFM steel is depicted in Fig 4.1.

4.3.2. Framework of microstructure based hybrid model

Once the RAFM steel is loaded in form of a component at high temperatures, there will be continuous degradation in microstructure and hence deterioration in strength with ongoing creep. The plastic strain accumulated due to the creep loading in material is accommodated by the movement of dislocations.

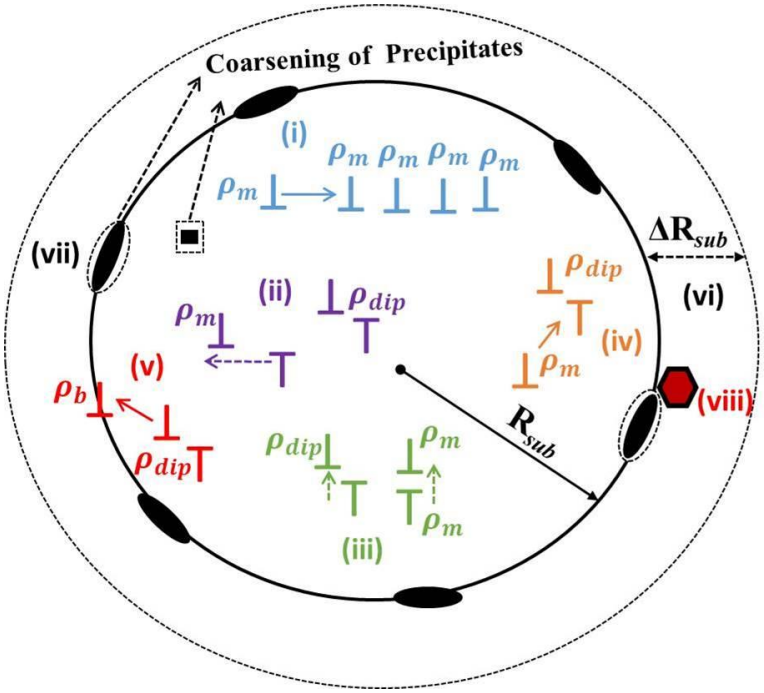

Figure 4.2. Different microstructural interactions inside a subgrain. (i) Signifies the production of mobile dislocations, (ii) Signifies glide/dynamic recovery of mobile and dipole dislocations, (ii) Signifies the Climb recovery of mobile and dipole dislocations, (ii) Signifies the Climb recovery

of mobile and dipole dislocations, (iv) Formation of dipole dislocations, (v) Conversion of the dipole dislocation in to boundary dislocations. (vi) ΔRsub signifies the subgrain growth, (vii) Coarsening of carbide and carbonitride precipitate and (viii) Represents the cavitation phenomena

Under the creep loading (in the dislocation creep regime), Frank-Read sources produce dislocations, recovery takes place due to the annihilation of dislocations, dipole forms, subgrains grow, precipitate coarsen and cavitation occurs, see Figure 4.2. Dislocation density plays an important role to determine the creep strain. The coupled various differential equations that are originally based on Ghoniem et al. [47], Basirat et al. [55] and Surya et al. [57, 58] and derived as per the aforementioned physical interactions and occurrences are presented in form of a hybrid creep model in Table 4.2.

The creep strain rate equation is concomitant with the Orowan equation that includes v_{gl}, ρ_m, M, and b, see Equation. (4.4) [47, 55, 164]. In this work two additional terms, i.e., precipitate damage D_{ppt} due to precipitate coarsening and cavitation damage D_{cav} due to creep cavitation are also incorporated in the denominator of Orowan equation [55, 58], see Equation. (4.4). The modification of Orowan equation was done on the basis of CDM approach. This modification is indispensable as the measured creep curve is manifested due to synergy of dislocation recovery, precipitate coarsening and cavitation.

Furthermore, the evolution of mobile dislocation density is represented in form of rate Equation (4.5), that includes the combined effect of the dislocation production term due to Frank-Read sources and negative terms due to immobilization of mobile dislocation at subgrain boundary, climb recovery and dynamic recovery [47]. $h_m = (\rho_m)^{-0.5}$ is the mobile dislocation spacing, ρ_{dip} is the dipole dislocation density. Similarly, the rate Equation (4.6) that deals with the evolution of dipole dislocation density includes the combined effect of the dipole production term and negative

terms representing conversion of dipole into boundary dislocations and dynamic recovery [47]. Herein, $h_b=1/[(\rho_m + \rho_{dip})R_{sub}]$ is the dislocation spacing within the subgrain boundaries [47].

The evolution of boundary dislocation density can be addressed by rate Equation (4.7), that embodied the production term due to formation of boundary dislocations from dipole dislocations and reduction terms due to annihilation of dipole dislocations, subgrain growth and Zener-pinning effect of precipitates at subgrain boundary [47]. Herein, M_{sb} is the mobility of subgrain boundary and can be defined by Equation. (4.8) that is comprised of lattice diffusion term and core mobility term. $P_{sb} = 4Gb^2\rho_b/3$ is the pressure on the subgrain boundary, $\xi = 0.30$ is a constant that deals with the conversion of the dipole configuration to boundary dislocation configuration, $\gamma_{sb}=4Gb^2\rho_bR_{sub}/3$ is the surface energy of subgrain boundary and N_{vi} is the number density of i^{th} precipitate. In Equation. (4.8), η is the transfer coefficient of dislocation core to jogs, D_{vp} is the core diffusion coefficient and D_s is the lattice self-diffusion coefficient. The rate Equation Equation. (4.9) that addresses subgrain growth is composed of incremental term that is multiplication of subgrain mobility and pressure and a reduction term due to the Zener-pinning effect of precipitates that are decorated at subgrain boundary [47]. Subgrain growth is aided by a reduction in subgrain boundary energy to stabilize the microstructure, whereas the growth is inhibited by the presence of precipitate and accounted by the Zener-pinning effect [47].

In the modified Orowan Equation (4.4), the employed damage or softening parameters are non-dimensional and their values lie between 0 and 1 and can be correlated through the occurrences of damage with microstructure evolution. Equations. (4.10 - 4.13) represent the rate equations related to precipitate coarsening and the associated softening/damage [47, 51, 55, 165]. In case of MX type precipitates l is considered to be 6 and l is equal to 4 for $M_{23}C_6$ type precipitates [47, 166]. In these equations, k_{pi} is a material constant and k_{di} is Ostwald coarsening constant and both vary with

the type of precipitates, temperature and stress [47, 51, 55, 165]. Cumulative softening due to all type of precipitates that are present in the system can be represented by Equation. (4.14), where *i = 1* and *2*, considering the aforementioned two precipitates. Similarly, rate equation for cavitation softening is comprised of material parameter *A*, strain ε and strain rate $\dot{\varepsilon}$ [44, 55, 165] and it can be represented in form of Equation. (4.15). done

Table 4.2. Creep model and corresponding set of equations

Equations	Number	Refs.
Modified Orowan equation $\frac{d\varepsilon}{dt} = \frac{b\rho_m v_{gl}}{M(1-D_{ppt})(1-D_{cav})}$	(4.4)	[47, 164, 167]
Rate equation for mobile dislocation density evolution $\frac{d\rho_m}{dt} = \underbrace{\frac{v_{gl}}{h_m}\rho_m}_{\substack{Frank\ read \\ source}} - \underbrace{\frac{v_{gl}}{2R_{sub}}\rho_m}_{\substack{Dipole \\ formation}} - \underbrace{8\left(\rho_m^{\frac{3}{2}} v_{cl}\right)}_{Climb\ recovery} - \underbrace{\left[d_{spon}(\rho_m + \rho_{dip})\rho_m v_{gl}\right]}_{Glide\ recovery}$	(4.5)	[47, 58]
Rate equation for dipole dislocation density evolution $\frac{d\rho_{dip}}{dt} = \underbrace{\frac{v_{gl}}{2R_{sub}}\rho_m}_{\substack{Dipole \\ formation}} - \underbrace{8\frac{v_{cl}}{h_b}\rho_{dip}}_{\substack{transformation\ of\ dipole \\ to\ boundary\ dislocation}} - \underbrace{d_{spon}\rho_m\rho_{dip}v_{gl}}_{Dynamic\ recovery}$	(4.6)	[47, 58]
Rate equation for boundary dislocation density evolution $\frac{d\rho_b}{dt} = \left[\underbrace{8\frac{v_{cl}}{h_b}\rho_{dip}}_{\substack{Formation\ of \\ boundary\ dislocation}} - \underbrace{\xi\,\rho_{dip}\left(\frac{v_{cl}}{h_b}\right)}_{\substack{Loss\ of\ dipoles \\ during\ transformation}} - \underbrace{\overbrace{M_{sb}\left(P_{sb} - 2\pi\left(\sum_{i=1}^{n} r_{mean,i}^2 N_{v,i}\right)\gamma_{sb}\right)}^{Zener\ drag}\frac{\rho_b}{R_{sub}}}_{Subgrain\ growth}\right]$	(4.7)	[47, 58]
Equation for subgrain boundary mobility $M_{sb} = \underbrace{\frac{2\pi\eta D_s\Omega}{bk_BT}}_{Core\ mobility} + \underbrace{\frac{2\pi bD_{vp}\Omega}{h_b^2 k_B T}}_{Lattice\ diffusion\ mobility}$	(4.8)	[47]
Rate equation for subgrain growth		

$$\frac{dR_{sub}}{dt} = \overbrace{\underbrace{M_{sb}\left(P_{sb} - 2\pi\left(\sum_{i=1}^{n} r_{mean,i}^2 N_{v,i}\right)\gamma_{sb}\right)}_{Subgrain\ growth}\frac{\rho_b}{R_{sub}}}^{Zener\ drag} \quad (4.9) \quad [47, 58]$$

Equation for damage rate due to coarsening of the precipitate

$$\dot{D}_{(ppt),l} = \frac{k_{p,i}}{(l-1)}\left(1 - D_{(ppt),i}\right)^{l} \quad (4.10) \quad [47, 55]$$

Damage due to precipitate coarsening

$$D_{(p),i} = 1 - \frac{r_{mean,i_{initial}}}{r_{mean,i}} \quad (4.11) \quad [52]$$

Generalized Ostwald ripening parameter equation

$$k_{p,i} = \frac{k_{d,i}}{\left(r_{mean,i_{initial}}\right)^{(l-1)}} \quad (4.12) \quad [52]$$

Ostwald ripening parameter equation

$$\dot{r}_{mean,i} = \frac{k_{d,i}}{(l-1)\left(r_{mean,i}\right)^{(l-2)}} \quad (4.13) \quad [52]$$

Cumulative damage parameter due to precipitates

$$D_{ppt} = \sum_{1}^{n}\left(D_{(ppt),i}\right) \quad (4.14) \quad [51, 58]$$

Damage rate due to cavitation

$$\dot{D}_{cav} = (A.\varepsilon.\dot{\varepsilon}) \quad (3.15) \quad [47, 55]$$

Equation for the dislocation glide velocity

$$v_{gl} = a_1\, exp\left(-\frac{Q}{k_B T}\right)\left[\frac{\Omega}{K_B T}\right]\sigma_{eff} \quad (4.16) \quad [47, 58]$$

Equation for the dislocation climb velocity

$$v_{cl} = \frac{D_s\, \Omega \sigma_{cl}}{b k_B T} \quad (4.17) \quad [168]$$

Effective stress

$$\sigma_{eff} = \sigma_{appl} - \sigma_{int} \quad (4.18) \quad [47, 51]$$

Internal stress

$$\sigma_{int} = \alpha M G_T b\sqrt{\rho_m + c_{dip}}\rho_{dip} \quad (4.19) \quad [47, 55]$$

Combined equation for climb velocity and climb stress

$$\sigma_{cl} + \frac{v_{cl}}{B_{vis}} = \frac{G_T b}{2\pi(1-\upsilon)} \frac{2}{d_{spon}+d_{dip}} \quad (4.20) \quad [55]$$

Dislocation mobility

$$B_{vis} = \frac{9\Omega D_s k_B T}{M C_0 G_T^2 b^7 \varepsilon_a^2 \, ln\left(\frac{r_2}{r_1}\right)} \quad (4.21) \quad [55, 154]$$

Dipole capture spacing

$$d_{dip} = \frac{M}{8\pi(1-\upsilon)} \frac{G_T b}{\sigma_{eff}} \quad (4.22) \quad [154]$$

$$\sigma_{cl} - v_{\mathrm{cl}} * N_1 = 0, where\ N_1 = \frac{b k_B T}{D_s \Omega} \quad (4.23) \quad \text{simplification of eq. 4.17}$$

$$\sigma_{cl} + v_{cl} * N_2 = N_3, where\ N_2 = \frac{1}{B_{vis}}\ , N_3 = \frac{G_T b}{2\pi(1-\upsilon)} \frac{2}{d_{spon}+d_{dip}} \quad (4.24) \quad \text{simplification of eq. 4.20}$$

$$\sigma_{cl} = \frac{N_3 * N_1}{(N_2+N_1)} \quad (4.25) \quad \text{from Eqs. 4.23 and 4.24}$$

Equation. (4.16) represents the mathematical model for glide velocity of the mobile dislocations that consists of calibration parameter a_1, activation energy for dislocation slip Q, atomic volume Ω, effective stress, Boltzmann constant and temperature [47]. Herein, effective stress is defined as the remaining amount of applied stress after subtracting the internal stress see Equation. (4.18). Internal stress is the resistance experienced due to the microstructure based ingredients that opposes the applied stress and hence retard the creep deformation [169]. Several researchers have proposed the different models to estimate the internal stress. Salazar et al. [170] and Ghoniem et al. [47] introduced the dipole dislocation density and precipitate to estimate internal stress. Barkar et al. [155] considered the internal stress due to mobile dislocation density and precipitate. In this research work, internal stress is considered to be composed of mobile dislocation density and dipole dislocation density [55], see Equation. (4.19). Further, climb velocity that is responsible for climb recovery, is defined by Equation. (4.17), that is interlinked with climb stress, solute diffusion coefficient, atomic volume, Burgers vector of dislocation, temperature and Boltzmann constant.

Herein, climb stress is described by Equation.(4.20) and it is associated with climb velocity, dislocation mobility B_{vis}, shear modulus , Burgers vector, Poisson's ratio, dipole annihilation distance, and dipole capture spacing [55]. Furthermore, the term dislocation mobility is represented by Equation.(4.21) and it is comprised of solute diffusion coefficient, atomic volume, Burgers vector, temperature, Boltzmann constant, Taylor factor, solute concentration C_0, shear modulus, outer cut off radius r_2, inner cut off radius r_1 and relative size misfit between solute and solvent atom ε_a [55, 154]. The dipole capture spacing is delineated by Equation. (4.22) that consist Taylor factor, shear modulus, Poisson's ratio, Burgers vector and effective stress [154]. Some scientific progress made in this work with respect to earlier reference models [47, 55, 58, 154] are discussed below,

(1) Temperature and time dependent mobility model for subgrain boundary migration is incorporated in the present approach, see Equation. (4.8).

(2) A more simplified method is presented to evaluate the climb velocity and associated equations are presented in form of variables N_1, N_2 and N_3 to obtain the climb stress and climb velocity, see Equations. (4.23-4.25).

(3) Temperature dependent shear modulus is incorporated, see Appendix 4.A.

(4) Evolution of additional variables that were not discussed in the literature, those are boundary dislocation spacing, subgrain boundary mobility, dipole capture spacing, climb stress, mean radius of MX (V and Ta based carbonitrides) precipitates, mean radius of $M_{23}C_6$ carbides is presented and discussed thoroughly.

(5) Evolution of damage due to two different types of precipitates is demonstrated separately.

4.4. Results and discussion

4.4.1. Creep Strain

Creep strain is simulated employing the modified Orowan Equation (4.4). Simulated and experimental creep curves are depicted and compared in Figures. 4.3a, b, c and d for various creep exposure conditions. It is found that simulated creep curves for all the four conditions are in reasonable agreement with experimental ones, up to the onset to tertiary creep regime.

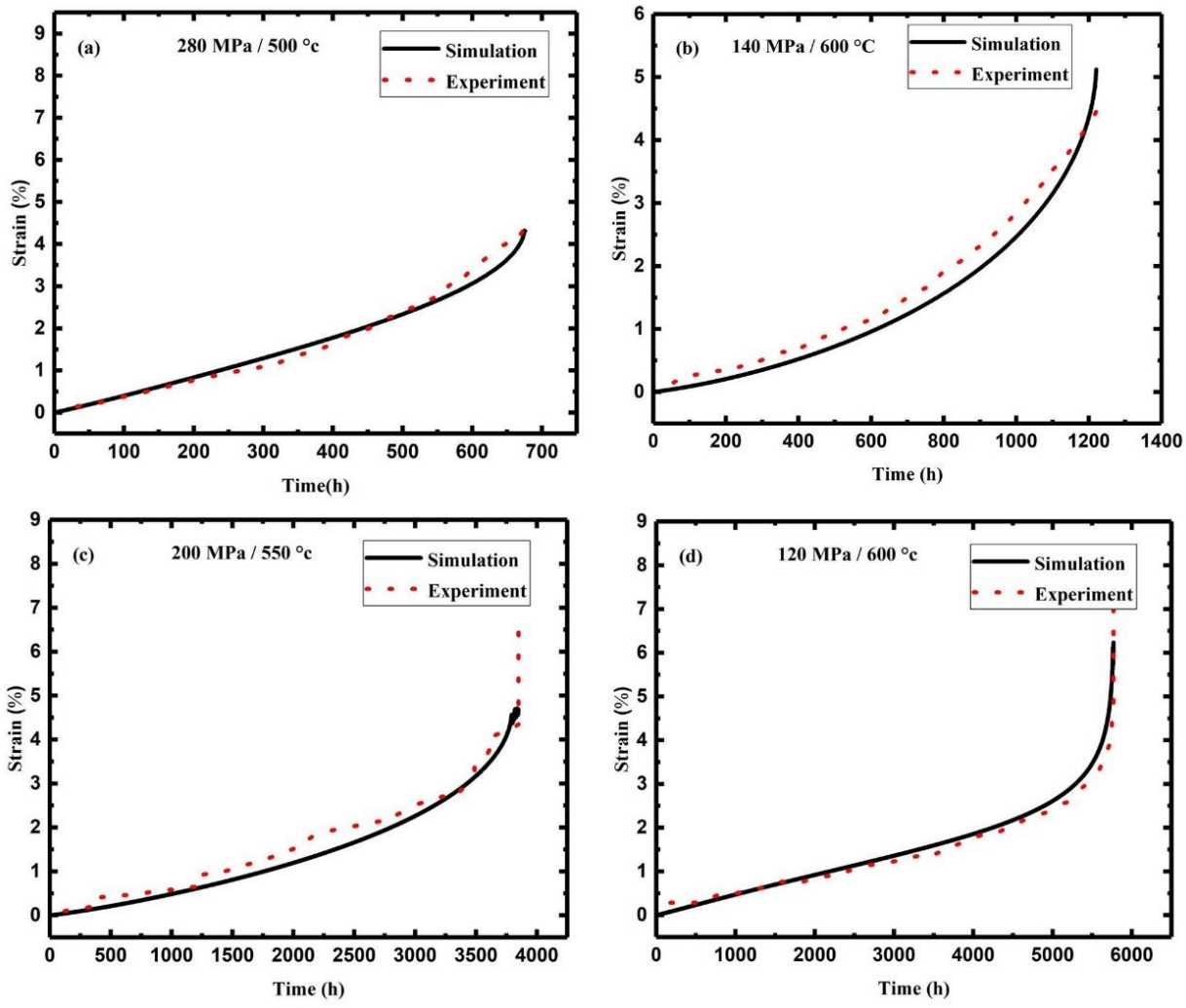

Figure 4.3. Simulated vs. experimental creep curves of RAFM steel at (a) 280 MPa / 500 ℃ (b) 140 MPa / 600 ℃, (c) 200 MPa / 550 ℃, (d) 120 MPa / 600℃. Experimental creep curves are obtained from literature [14, 161, 162].

Vanaja et al. [40] studied the creep deformation behavior of RAFM steel and a short primary creep regime, extended tertiary stage and negligible secondary creep regime was reported, as also demonstrated by herein simulated curves. Higher stress resulted in higher creep rate that weakens the material and finally led to an early stage of failure, see Figures. 4.3b and d [47, 171, 172].

4.4.2. Substructure evolution led by creep

The evolution of mobile dislocation density, dipole dislocation density, boundary dislocation density and subgrain radius as the function of creep exposure time is depicted in Figures. (4.4a, 4.5a), Figures. (4.4b, 4.5b), Figures. (4.4c, 4.5c) and Figures. (4.4d, 4.5d), respectively. It is also tangible from Figures. (4.4a, 4.5a) that the mobile dislocation density is high in the beginning and later on the reduction is observed with the ongoing creep due to the spontaneous annihilation led by glide and climb recovery as well as production of new dipoles [49, 58]. Similarly, the dipole dislocation density is also high at the start of the creep and decreases with the exposure time (see Figures. (4.4b, 4.5b)). *The decrease in the number of mobile and dipole dislocation density is rapid initially, due to high annihilation rates led by high stored elastic energy. Afterwards, this reduction rate decreases due the relaxation of the substructure with less stored elastic energy and low annihilation rates.* The pre-existing dipole and newly formed dipoles are converted into boundary dislocation. This is the reason that boundary dislocation density is high during the beginning of the creep and afterwards decreases as the domination of subgrain growth leads to its reduction, see Figures. (4.4c, 4.5c). At the end of the numerical simulation, the predicted values of mobile, dipole and boundary dislocation densities lie in the range of 1.91×10^{13} - 3.08×10^{14} m^{-2}, 1.27×10^{11} – 4.07×10^{12} m^{-2} and 2.89-4.64×10^{14} m^{-2}, respectively, for the explored conditions.

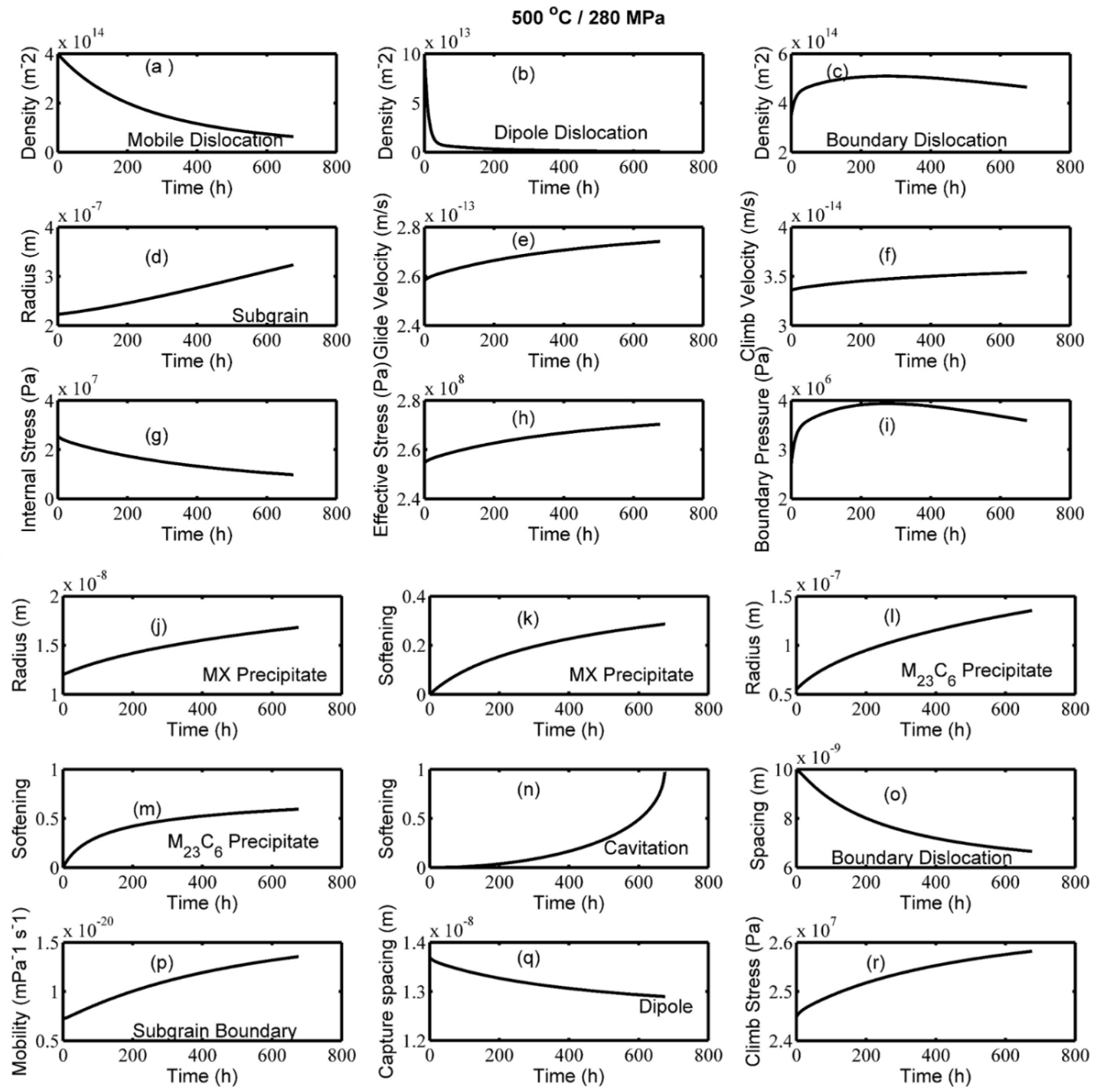

Figure 4.4. Output parameters of model vs. time curves for 500 ℃ / 280 MPa (a) Mobile dislocation density, (b) Dipole dislocation density, (c) Boundary dislocation density, (d) Subgrain radius, (e) Glide velocity, (f) Climb velocity, (g) Internal stress, (h) Effective stress, (i) Boundary pressure, (j) Radius of MX precipitate, (k) Softening of MX precipitate, (l) Radius of $M_{23}C_6$ precipitate (m) Softening of $M_{23}C_6$ precipitate, (n) Cavitation softening, (o) Boundary dislocation spacing, (p) Subgrain boundary mobility, (q) Dipole capture spacing and (r) Climb stress

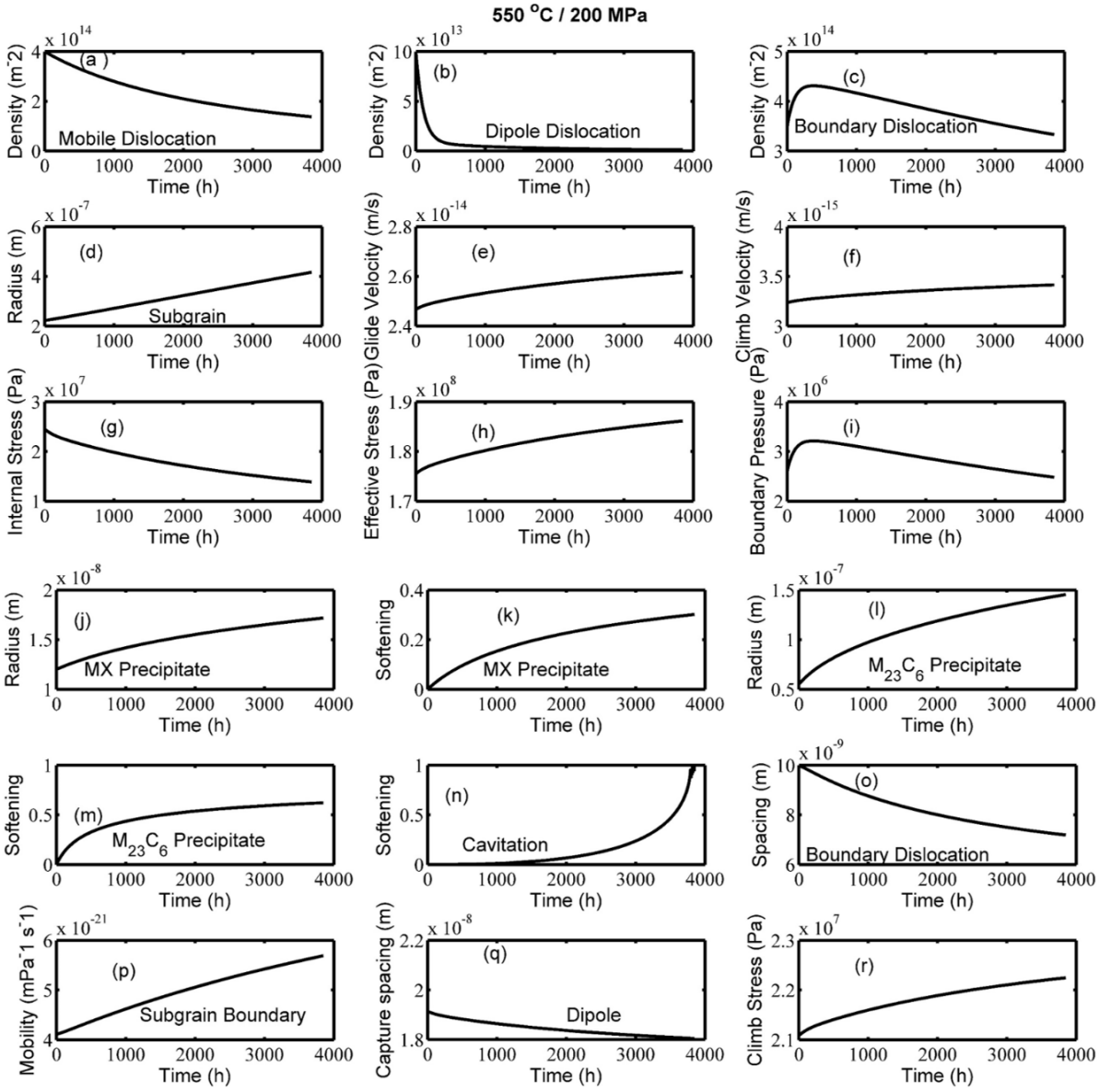

Figure 4.5. Output parameters of model vs. time curves for 550 ℃ / 200 MPa (a) Mobile dislocation density, (b) Dipole dislocation density, (c) Boundary dislocation density, (d) Subgrain radius, (e) Glide velocity, (f) Climb velocity, (g) Internal stress, (h) Effective stress, (i) Boundary pressure, (j) Radius of MX precipitate, (k) Softening of MX precipitate, (l) Radius of $M_{23}C_6$ precipitate (m) Softening of $M_{23}C_6$ precipitate, (n) Cavitation softening, (o) Boundary dislocation spacing, (p) Subgrain boundary mobility, (q) Dipole capture spacing and (r) Climb stress

TEM micrograph of RAFM steel reported by Vanaja et al. [162] showed that the average dislocation density is ~0.812 × 10^{13} m^{-2} after creep deformation at 550 ℃ / 200 MPa. Similarly, TEM micrograph of RAFM steel reported by Laha et al. [11]showed that the average dislocation density is ~1.656 × 10^{13} m^{-2} after creep deformation at 550 ℃ / 220 MPa. The predicted values of dislocation densities from the model are comparable with these experimental values and it can be noted that the order of magnitude lies in the same range, see Table 4.3. Several works have been accomplished in the past that are related to the creep deformation of 9 % Cr steels and the corresponding dislocation densities were reported.

In case of HT-9 ferritic-martensitic steel, Wen et al. [163] showed that the dislocation density in cell and cell wall were in the range of ~ 6 × 10^{12} - 8 × 10^{13} m^{-2} and ~ 3× 10^{14} m^{-2}, respectively, at varying temperature 490-600 ℃ and stresses 9-173 MPa. In case of P91 steel, Spigareli et al. [173] observed the free dislocation density to be ~ 1 × 10^{14} m^{-2} at 600 ℃ / 70 MPa. Similarly, for another 9 % Cr steel, Magnusson et al. [49] predicted the free dislocation and immobile dislocation density to be ~ 8 × 10^{11} m^{-2} and ~ 7 × 10^{12} m^{-2}, respectively at 650 ℃ / 104 MPa. Panait et al. [174] investigated the dislocation density for P91 steel after the creep at 600 ℃ / 80 MPa and reported that 1.8 ± 1.7 × 10^{14} m^{-2}. Similarly, in case of Cu-16at % Al, Orlová et al. [175] reported the dislocation density to be ~ 2× 10^{13} m^{-2} at 450 ºC / 39.2 MPa . Mobile, static and boundary dislocation density in hot work tool steel at 500 ℃ / 370 MPa is predicted to be ~ 5× 10^{11} m^{-2}, ~ 3 × 10^{10} m^{-2} and 1 × 10^{12} m^{-2}, respectively[164]. Argon et al. [176] reported the strain dependent dislocation density in the subgrain boundaries and in the subgrain interior of iron to be ~ 7 × 10^{8} cm^{-2} and ~ 8 × 10^{9} cm^{-2} , respectively, after the creep at 600 ℃ / 75 MPa. Argon et al. [176]reported the strain dependent dislocation density in the boundaries of deformed copper single crystal to be 1.5 × 10^{14} m^{-2} after the annealing at 0.3T_m, where T_m is melting point of copper. Riedlsperger et

al. [159] predicted the mobile, static and boundary dislocation density to be ~ 1.2× 10^{13} m^{-2}, ~ 1.3 × 10^{10} m^{-2} and ~ 6.0 × 10^{14} m^{-2}, respectively, at 650 ℃ / 70 MPa in P91 steel. Surya et al. [58] reported the mobile, dipole and boundary dislocation density to be ~ 1 × 10^{14} m^{-2}, ~ 0.1 × 10^{14} m^{-2} and ~ 2.5 × 10^{14} m^{-2}, respectively, for 9 % Cr steel at 600 ℃ / 145 MPa. Above discussion clearly suggests that dislocation density strongly depends on the materials, processing and exposure conditions in terms of stress, temperature and strain.

Table 4.3. Dislocation densities and subgrain radius at the end of the creep/simulation

Parameters	Simulation result				Experimental data
	500 ℃ / 280 MPa	600 ℃ / 140 MPa	550 ℃ / 200 MPa	600 ℃ / 120 MPa	500-550 ℃ / 200-220 MPa
Mobile dislocation density (m^{-2})	6.31×10^{13}	3.08×10^{14}	1.37×10^{14}	1.91×10^{13}	0.8-1.6 × 10^{13} Refs. [11, 162]
Dipole dislocation density (m^{-2})	4.39×10^{11}	4.07×10^{12}	1.16×10^{12}	1.27×10^{11}	--
Boundary dislocation density (m^{-2})	4.64×10^{14}	4.06×10^{14}	3.32×10^{14}	2.89×10^{14}	--
Subgrain radius (m)	3.23×10^{-7}	3.08×10^{-7}	4.16×10^{-7}	4.58×10^{-7}	2.96-4.11 × 10^{-7} Refs. [11, 162]

The radius of subgrain with ongoing creep and predicted through model is demonstrated in Figures. (4.4d, 4.5d). It can be observed that subgrain size is increasing with ongoing creep due to the recovery [97, 177, 178]. The subgrain radius was increased from 0.225 μm to 0.308-0.458 μm, for varying creep conditions, see Table 4.3. The TEM micrographs of Vanaja et al.[162] shows that

the subgrain radius for RAFM is ~ 0.411 µm after the creep at 550 ℃ / 200 MPa. Similarly, Laha et al. [11] reported that the subgrain radius for RAFM steel to be ~ 0.296 µm after creep at 550 ℃ / 220 MPa. In case of P91 steel, Spigareli et al. [173] reported the subgrain radius to be 0.4 µm at 600 ˚C / 70 MPa. The predicted magnitude of subgrain radius are compared with these experimental values and the magnitude lies in the similar range, see Table 4.3.

Furthermore, at the end of numerical simulation the model predicts that $M_{23}C_6$ (M=Fe, Cr) carbides precipitate radius reaches up to 135.3-151.6 nm and MX (M=V, Ta and X=C and N) carbonitrides precipitate radius reaches up to 16.8-18.7 nm, for varying creep conditions (see Figures. 4.4j, l and 4.5j, l). Vanaja et al. [162] reported that the mean radius of $M_{23}C_6$ carbides precipitate increased up to 145 nm at 550 ℃ / 200 MPa and no appreciable change in the MX carbonitrides is observed for RAFM steel. Similarly, for another RAFM steel, Chen et al. [10] reported that the mean radius of precipitates, i.e., MX and $M_{23}C_6$ increased up to 22.4 nm and 90.45 nm, respectively at 550 ℃ / 180 MPa. The predicted values of both type of precipitates in this work (carbides and carbonitrides) are comparable with these experimental values and the magnitude lies in same range. Based on these observations the substructure evolution with ongoing creep is depicted in Figure.4.6, where initial high density of dislocations and precipitates are demonstrated before the creep, whereas after the creep, microstructure with cavities, coarse precipitates and less dislocations density is also delineated.

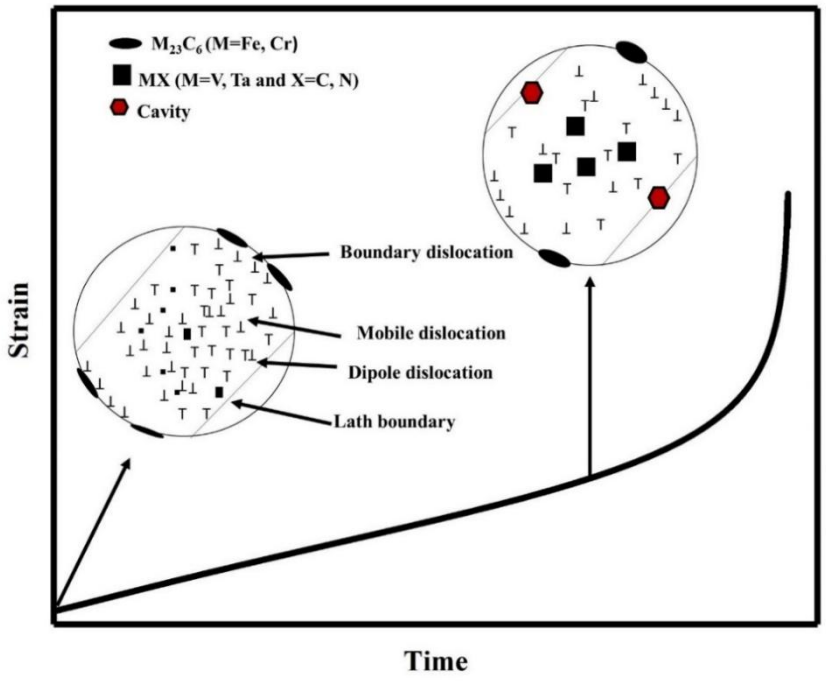

Figure 4.6. Schematic diagram of the proposed substructure evolution during creep of RAFM steel

4.4.3. Creep led changes in internal stress, effective stress, climb stress, glide velocity, climb velocity and dipole capture spacing

Model predicted internal stresses for varying creep conditions are depicted in Figures. (4.4g and 3.5g). It can be observed that its magnitude is decreasing with the ongoing creep and that can be correlated with the decrease in the dislocation density as discussed in Section 3.4.2. In the present work, internal stress is predicted to be in the range of 4.9-20.20 MPa at the end of creep/numerical simulation. Whereas, the research article published by Orlová et al. [175] suggested that the internal stress is found to be 10 % or more of the applied stress and it was found to be ~ 78 MPa at 400 °C / 196 MPa for α iron. In case of P9 steel, Christopher et al. [179] reported the internal stress in the range of ~56-114 MPa at 600 ^{o}C / 63-150 MPa. In another work on P9 steel, Christopher et al.[180] reported the internal stress to be 55 MPa at 600 ^{o}C / 80 MPa. Similarly, for

P91 steel, Christopher et al. [181] reported the internal stress to be 125 MPa against 1.3% strain at 600 ℃. In case of P92 steel, Surya et al. [58] reported the internal stress to be in the range of 8 - 13 MPa at the end of numerical simulation for different conditions, i.e., 145-160 MPa / 600 ℃. In tempered martensitic steels the high initial dislocation density leads to high internal stresses in the beginning of creep[97, 177, 178, 182]. Aforementioned, literature reported data on the internal stress support our predicted internal stresses in such a way that both are in the similar range and comparable. The predicted evolution of effective stress is shown in Figures. 4.4h and 4.5h for the varying creep conditions. It can be seen that the magnitude is increasing with ongoing creep that occurs due to decrease in internal stress led by reduction in dislocation density. In this work, the effective stress at the end of creep/numerical simulation is observed to be in the range of 115-270 MPa. In case of P9 steel, Christopher et al. [179] reported the effective stress in the range of ~5-35 MPa at 600 ^{o}C / 63-150 MPa. In another study on P9 steel, Christopher et al.[180] predicted the effective stress to be 5 MPa at 600 ^{o}C / 80 MPa. Similarly, for P91 steel, Christopher et al. [181]reported the effective stress to be 25 MPa against the 1.3 % strain at 600 ℃. In case of P92 steel, Surya et al. [58] reported the effective stress in range of ~ 134-149 MPa at the end of numerical simulation for 600 ℃ / 145-160 MPa. The magnitude of predicted effective stress herein is found to have a similar order of magnitude that has been reported in the literature [58].

Predicted dipole capture spacing for varying creep conditions with ongoing creep is depicted in Figures. 4.4q and 4.5q. It can be noticed that the magnitude is decreasing with ongoing creep. This is due to the fact that dipole capture spacing is inversely related with the effective stress. As the effective stress increases it would lead to decrease in the dipole capture spacing. In this research work dipole capture spacing is observed to be in the range of 13-28 nm for varying explored conditions. Basirat et al.[55] reported the value of dipole capture spacing in the range of 12-16 nm

for 9 % Cr steel for a stress range of 100-200 MPa. In the research article of Rollett et al. [183], the ratio of dipole capture spacing to mean dislocation spacing is reported to be 0.13. The ratio of dipole capture spacing to mobile dislocation spacing obtained herein, is in the range 0.10-0.47 and it is in line with Rollett et al. [183].

Prediction of climb stress with ongoing creep is depicted in Figures. 4.4r and 4.5r at varying creep conditions. It can be observed that its magnitude is increasing with ongoing creep, since it is inversely related with the dipole capture spacing. In the current research work the climb stress at the end of numerical simulation is estimated in the range of 17.16-25.8 MPa for explored conditions. Hamada et al. [184] reported the climb stress in the range of 3.2 - 10.1 MPa for 9 Cr-1 Mo steel without Nb, V and with Nb, V, respectively at 600 ℃ / 180 MPa. The predicted results herein are found to be slightly higher from the aforementioned literature values, however the order of magnitude lies in the similar range. The climb stress in these materials can be very much dependent on elements contributing to solid solutions. In RAFM steel, there are additional solid solution strengtheners such as W and Ta in addition to V and Nb. Hence, the predicted range of climb stress is higher than literature reported climb stresses [184].

The predicted evolution of the glide velocity for different conditions is depicted in Figures. 4.4e and 4.5e. Its magnitude is increasing with the creep exposure time, as it is directly influenced by the effective stress having the same tendency. In the present research work the glide velocity is observed to be in the range of 2.62×10^{-14}-2.74×10^{-13} m/s for the different creep conditions. Panait et al. [174] investigated the mean dislocation velocity and reported 2×10^{-15} m/s for P91 steel at 600 ℃ / 80 MPa. Riedlsperger et al. [159] predicted the glide velocity to be ~ 7.6×10^{-13} m/s for P91 steel at 650 ℃ / 70 MPa. In another study on P91 steel, Surya et al.[57] predicted the glide velocity in the range of ~ 3.9×10^{-15} - 3.42×10^{-14} m/s at 600 ℃ / 80-120 MPa. Eisenlohr et

al. [185] performed the stress dip test to predict the dislocation glide velocity in case of pure magnesium as well as alloy AS21 and reported the range to be 10^{-10} - 10^{-4} m/s at 200-400 ℃ / ~1-26 MPa. Johnston and Gilman [186] performed a test to determine the dislocation glide velocity and dislocation density in lithium fluoride crystal. They observed that the dislocation glide velocity of edge component is extremely sensitive to the applied stress and it was found to be in the range of 10^{-9} – 10^{3} m/s for wide range of stresses, i.e., 6 - 200 MPa [186]. Stein et al. [187] estimated the dislocation velocity for iron with 3.25 percent silicon, in the range of ~ 2×10^{-9} - 1×10^{-4} m/s at 100 ℃ / 100-150 MPa. George et al.[188] emphasized the stress, temperature and impurity concentration dependency of dislocation velocity in an intrinsic silicon semiconductor and reported the magnitude to be in the range ~ 1×10^{-9}- 8×10^{-6} m/s at 520 ℃- 800 ℃ / 30 MPa. It was explored that the dislocation velocity depends on the temperature and the phosphorous concentration. For the phosphorous concentration of 1.4×10^{19} at.cm^{-3} and temperature range 520 ℃- 710 ℃, velocity was found to be in the range of ~ 5×10^{-8}- 8×10^{-6} m/s. The above discussion leads to the fact that, the dislocation glide velocity depends on material, stress, and temperature and impurity concentration. Also, it can be noted that predicted range of glide velocity herein is in line with the literature data [57, 159, 174]. The predicted climb velocity at varying conditions with ongoing creep is depicted in Figures. 4.4f and 4.5f. It can be observed that its magnitude is increasing slowly with creep, since it is directly related with the climb stress that shows the similar evolution behavior as discussed previously. Herein, climb velocity was found to be in the range of 3.41×10^{-15}-3.53×10^{-14} m/s for the explored creep conditions. Turunen et al. [189] predicted the dislocation climb velocity in pure aluminium to be in the range of ~ 8×10^{-10} - 5×10^{-4} m/s with varying vacancy concentration as well as temperature that are 5×10^{-8}- 1×10^{-2} ccm^{-1} and 200 - 659 ℃, respectively. Edelin et al. [190] estimated the dislocation climb velocity in magnesium to be

in the range of ~ 8×10^{-9} -9×10^{-6} m/s at 325-496 ºC / 18 MPa. In case of heavily deformed body centered cubic iron, Kabir et al.[191] predicted the climb velocity to be in the range of ~ 5×10^{-5} - 15×10^{-3} m/s at 527 ºC / 750-2500 MPa. In case of Fe-Au alloy, Versteylen et al. [192]reported the dislocation climb velocity to be ~ 8×10^{-11} m/s at 550 ℃ / 100 MPa. For P91 steel, Riedlsperger et al. [159] predicted the climb velocity to be ~ 1.63×10^{-13} m/s at 650 ℃ / 70 MPa. Similarly, for another 9 % Cr steel, Surya et al. [57] reported the value of climb velocity in the range of ~ 5×10^{-16} – 4.14×10^{-14} m/s at 600 ℃ / 80-120 MPa. From the above discussion it may be concluded that climb velocity strongly depends on materials, stress, and temperature and vacancy concentration. Our predicted results in terms of climb velocity are in line with the literature data [57, 159].

4.4.4. Evolution of subgrain boundary mobility, boundary dislocation spacing and boundary pressure

The evolution of subgrain boundary mobility with ongoing creep is depicted in Figures. 4.4p and 4.5p for explored creep conditions. It can be seen that the mobility of subgrain is increasing with creep. *This is due to the fact that at the beginning of the creep, the boundary dislocation spacing decreases due to the accumulation of boundary dislocations. This leads to increase in the stored energy inside the subgrain boundaries. In order to reduce this stored energy, the mobility of the subgrains increases in combination with recovery in order to reduce the surface energy per unit volume.* On the other hand, there is a continuous degradation in pinning effect due to the precipitate coarsening at later stages. Therefore, less number of obstacles are available to hinder the subgrain boundary migration[192]. *In the other words, precipitate coarsening (at subgrain boundary) leads to increase in the inter precipitate spacing and thus the effective barriers for subgrain boundary motion are reduced and leads to increase in the subgrain mobility* [47]. In this work, at the end of

the numerical simulation/creep, the subgrain mobility was found to be in the range of 5.01×10^{-21}-1.35×10^{-20} $mPa^{-1}s^{-1}$ for the explored conditions. Winning et al. [193] measured the subgrain boundary mobility and reported that 4.5×10^{-16} $mPa^{-1}s^{-1}$ and 5×10^{-10} $mPa^{-1}s^{-1}$ at 200 ^{o}C and 600 ^{o}C, respectively. In case of Al-0.1 % Mn, Fabrice et al. [194] reported that the mobility of subgrain boundaries lies in the range of ~ 6×10^{-17} $mPa^{-1}s^{-1}$ - 5×10^{-15} $mPa^{-1}s^{-1}$at 143-315 ^{o}C. In case of Al-0.05 % Si , Humphery et al. [72] reported that the mobility of subgrain boundaries (2.5-6 degree) for 300 Goss orientation lies in the range of ~ 3×10^{-16} -3×10^{-14} $mPa^{-1}s^{-1}$. Similarly, for 400 Goss orientation and 2.5-6 degree misorientations, mobility lies in the range of ~ 3×10^{-14} -3×10^{-12} $mPa^{-1}s$. In case of P92 steel, Surya et al. [58] reported that the mobility of subgrain boundaries to be 0.9×10^{-20} $mPa^{-1}s^{-1}$ and 1.16×10^{-20} $mPa^{-1}s^{-1}$ at 600 °C and 650 °C, respectively. Above discussion suggests that mobility of subgrain boundary is dependent on the material, temperature, stress, misorientation angle and texture. Prediction of subgrain mobility in this work is coherent with literature reported data [58].

The evolution of boundary dislocation spacing with creep exposure time is depicted in Figures. 4.4o and 4.5o at varying creep conditions. Its trend is found to be decreasing with ongoing creep. It is known that boundary dislocation spacing strongly relies on both dislocation densities, mobile and dipole that transform to boundary dislocations. Over the period of time more mobile and dipole dislocations are transformed to boundary dislocations and hence leading to decrease in spacing. In this work, at the end of the numerical simulation/creep, the boundary dislocation spacing is found to be in the range of 6.65-7.52 nm for the explored conditions. Eisenlohr et al. [195] studied the dislocation spacing and cell size in case of single crystal CaF_2 and estimated that the average dislocation spacing lies in the range of ~ $2.1\text{-}2.9 \times 10^{-6}$ m for 800 °C - 857 °C /1.6-4.1 MPa. From

the above reported data, it may be concluded that the boundary dislocation spacing is dependent on the material in addition to temperature, strain and stress.

The evolution of boundary pressure with creep exposure time is depicted in Figures. 4.4i and 4.5i for the varying creep conditions. The magnitude is found to be increasing initially and afterwards decreases with ongoing creep. As discussed in Section 4.4.2, it is directly influenced by the population of boundary dislocations present in the subgrain boundary and thus follows the trends of boundary dislocation density. At the end of the numerical simulation, it's magnitude is found to be in the range of 2.06-3.58 MPa for the explored creep conditions. Humphery et al. [72] reported that the subgrain boundary pressure to be ~0.6 MPa in case of low angle grain boundaries. In case of P92 steel, Surya et al. [58] predicted the boundary pressure in the range of ~ 1.4 – 2.8 MPa at 650 ℃ / 92-110 MPa. It is clear from the reported data that the prediction of boundary pressure has a similar range and order of magnitude reported in literature [58].

4.4.5. Occurrence of damage due to precipitate coarsening and cavitation

The evolution of damage due to the MX carbonitrides and $M_{23}C_6$ carbides is depicted in Figures. (4.4k, 4.5k) and Figures. (4.4m, 4.5m), respectively, for the explored conditions. It can be visualized from the aforementioned figures that damage or softening due to different type of precipitates is increasing with creep. The damage due to precipitates is correlated with coarsening of the precipitates as discussed in Section 3.4.2. Coarsening of precipitate occurs in such a way that large precipitates becomes larger at the expense of other precipitates, hence decreasing the number density. *This is attributed to the minimization of the surface area of precipitates normalized by volume to decrease the energy of the system.* In the present work, the damage rate due to the MX carbonitrides is evaluated to be in the range of $2.80 \times 10^{-5} – 2.29 \times 10^{-4}$ h^{-1} for the explored conditions. Similarly, the damage rate due to the $M_{23}C_6$ carbides is estimated in the range

of 3.09×10^{-5} – 2.78×10^{-4} h^{-1} for the explored conditions. In case of P9 steel, Christopher et al. [196] reported that the collective damage rate due to all type of precipitates to be $\sim 2.17 \times 10^{-5}$ h^{-1} for 600 ºC / 60 MPa. In case of P92 steel, Surya et al. [58] reported that the collective damage rate due to all type of precipitates lies in the range of $\sim 8.00 \times 10^{-5} – 1.33 \times 10^{-4}$ h^{-1} for 600 ºC / 145-160 MPa. Similarly for P91 steel, Surya et al. [57] reported that the collective damage rate due to all type of precipitates lies in the range of $\sim 5.26 \times 10^{-6} – 1.11 \times 10^{-5}$ h^{-1} for 600 ºC / 80-120 MPa. From the above discussion it can be said that the predicted damage rate due to precipitates is following the literature data. The starting values of parameters k_{d1} and k_{d2} were collected from the literature and optimized in such a way that the predicted size of the MX carbonitrides and $M_{23}C_6$ carbides become comparable with the experimental results.

Evolution of creep cavitation softening/damage due to formation of creep cavities is depicted in Figures. (4.4n, 4.5n) for the explored conditions. It can be seen that cavitation softening is accelerating with creep due to increase in strain and strain rate that leads to continuous formation and growth of cavities. Damage parameters attaining the value 0.99 represents the state that specimen is about to fail [197]. The presence of coarsened second phase particles, i.e., laves and carbides situated on the high angle grain boundaries triggers the creep cavitation. Cavity nucleation starts from the very beginning of the creep and it grows over the period of the exposure [198]. It is also reflected from the cavitation damage evolution curves that, in the beginning, the magnitude of damage is low, as cavities have just nucleated. Over the period of time cavities growth accelerates, leading to increase in damage rate and finally coalescence of cavities takes places in the tertiary regime and corresponding rapid increase in cavitation damage can be evidenced. In the current work, predicted cavitation damage rate is found to be in the range of 2.74×10^{-5} – 4.54×10^{-4} h^{-1} for the explored conditions. In case of 316 L austenitic stainless steel, Christopher et al.

[199] predicted the characteristic damage rate in the range ~ 8×10^{-6} - 4×10^{-3} h^{-1} at 650 ^{o}C / 110-240 MPa. In case of P92 steel, Surya et al. [58] reported the cavitation damage rate in the range of ~ 2.08×10^{-5} – 4.17×10^{-5} h^{-1} at 600 ^{o}C / 145-160 MPa. Similarly, for P91 steel, Surya et al. [57]reported that the cavitation damage rate lies in the range of ~ 1.01×10^{-6} – 2.04×10^{-5} h^{-1} for 600 ^{o}C / 80-120 MPa. From the above discussion, it can be said that the predicted cavitation damage rate is in line with the literature data [57, 58, 199].

4.4.6. Influence of applied stress on model parameters

The influence of applied stress on the end values of dislocation densities (mobile, dipole, and boundary) can be seen from the Figures. (4.7a, 4.7b and 4.7c), respectively, for 600 ^{o}C / 140 MPa and 600 ^{o}C / 120 MPa. In all three cases of dislocation densities, the magnitude is high at the higher stress as the *more applied stress results in to the production of more dislocations*. Similarly, the influence of stress on the internal stress can be seen from the Figure. 4.7g. It is concomitant with the evolution of dislocations, which is high at higher stress as discussed above. The influence of applied stress on the effective stress can be seen from the Figure. 4.7h. The magnitude can be found high at the higher stress, as it is directly related to the applied stress. Similarly, climb stress has been observed to be having high magnitude at the higher applied stress (see Figure. 4.7r) as it follows the trend of effective stress. The effect of applied stress on the glide velocity and climb velocity can be noticed from Figure. 4.7e and 4.7f, respectively. It can be observed that, their magnitude is higher at the higher stress, since, they are directly correlated with effective and climb stresses, respectively, that are high at higher stress. The impact of applied stress on the dipole capture spacing can be assessed from Figure. 4.7q. It can be observed that its magnitude is high at the lower applied stress, since, it is inversely correlated with effective stress/applied stress. The

influence of applied stress on the subgrain size can be seen through the Figure. 4.7d. Subgrain size is high at the lower stress and it is in line with the literature [58].

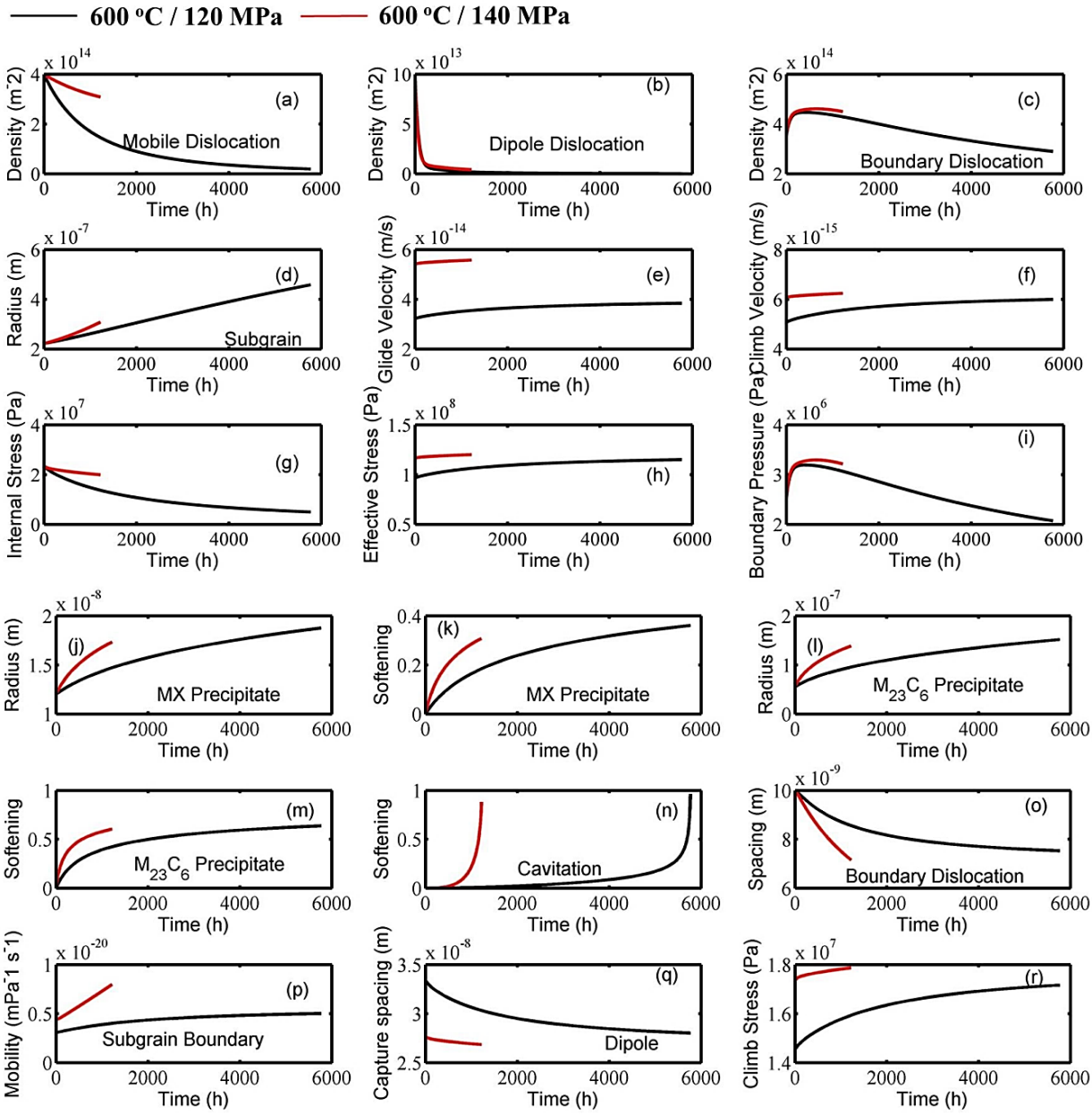

Figure 4.7.Influence of stress 120 MPa 140 MPa on the modeled parameter at 600 ℃ (a) Mobile dislocation density, (b) Dipole dislocation density, (c) Boundary dislocation density, (d) Subgrain radius, (e) Glide velocity, (f) Climb velocity, (g) Internal stress, (h) Effective stress, (i) Boundary

pressure, (j) Radius of MX precipitate, (k) Softening of MX precipitate, (l) Radius of $M_{23}C_6$ precipitate (m) Softening of $M_{23}C_6$ precipitate, (n) Cavitation softening, (o) Boundary dislocation spacing, (p) Subgrain boundary mobility, (q) Dipole capture spacing and (r) Climb stress

The influence of applied stress on the subgrain boundary dislocation spacing is depicted in Figure. 4.7o. It can be observed that the magnitude is high at the lower stress as it is inversely related with dislocation density that is low at lower stress and hence it leads to higher spacing. The influence of applied stress on the subgrain boundary mobility is depicted in Figure. 4.7p. It can be observed that the magnitude of subgrain boundary mobility is high at the higher stress as it inversely depends on the boundary dislocation spacing which is low at higher stress. The influence of applied stress on the boundary pressure is depicted in Figure.4.7i. It can be observed that the magnitude of boundary pressure is high at the higher stress and as it can be correlated with high boundary dislocation density.

The influence of applied stress on the size of both type of precipitates and respective damage is depicted in Figures. (4.7j, 3.7k) and Figures. (4.7l, 7m), respectively. It can be observed that the coarsening rate of both type of precipitates is high for the higher applied stress. It is established that, at higher stress the dislocation density is high and as the dislocations act as the source and sink for the vacancies, the substructure evolved at high stress with high dislocation density facilitate the diffusion more easily. Furthermore, as the jump frequency of the atoms can be altered and enhanced by the influence of stress, it may lead to the high coarsening rate at higher stress. Since, the specimen exposed to higher stress failed early than specimen at lower stress due to cumulative and localized damage, the final precipitate size and precipitate damage has smaller magnitudes at higher stress compare to low stress exposed specimens. The main driving force for the coarsening is reduction in free energy due to decrease in surface area per unit volume and the

damage parameter accounts for this mechanism. It can be observed that, at the end of simulation, the magnitude of damage due to both type of precipitates is high for the specimen exposed to lower stress, as it was exposed to larger period of time. Similarly, the influence of applied stress on the cavitation softening/damage is depicted in Figue.3.7n. It can be observed that the cavitation softening is accelerating towards the value 1 that represents the failure of the specimen, rapidly at higher stress. This suggests that the high stress leads to the more profound creep and associated cavitation reliant localized damage.

4.5. Significance and effectiveness of the model

The model demonstrates an easy computation method for estimating the climb velocity. Thus, it requires less parameters and relatively small computational effort. Furthermore, as the mobility model is more realistic in terms of time and temperature dependency, it would lead to more accurate predictions of microstructural ingredients compared to other models [57, 58]. It is well established that cavitation and recovery of substructure starts at very early stages and continue with ongoing creep in 9–12% Cr steels. As this model demonstrates the evolution of each parameters and tracks their magnitude in each time step of deformation, provides an insight about the material degradation during creep. Model output suggest that all three types of dislocation densities are decreasing, subgrains are growing and precipitate coarsening is taking place with the creep. This leads to the softening of the material, as the enhanced mobility and growth of subgrains with coarsened precipitates, decrease the resistance offered by material under creep exposed condi tions. This further suggests that the materials should be designed in a way so that the aforementioned occurrences can be delayed. The model can be more effective in designing of new high temperature materials as well as estimating their creep life, when it works in synergy with pre cipitation kinetic software and a cavitation model [57, 58, 171]. The area fraction of the cavities

that formed during creep would be the output of the cavitation model that will facilitate to estimate the effective load bearing area of the material in each time step. Influence of chemical composition and heat treatment shall be available from the precipitation kinetic software for each time step. Initial dislocation density of the material can be simulated employing models that deals with martensitic transformation, i.e., TTSD model [200]. Now the dislocation density, precipitation state as per the composition and heat treatment and load bearing section can be updated in this creep model in each time step. Thus, the model would lead to estimate the near creep life of a proposed alloy. Now, altering the microstructure through composition and heat treatment the design of new alloys would be facilitated through this approach

4.6. Summary and conclusions

In this research work, the creep curves of RAFM steel adopted from the literature are simulated employing an improved creep model. The model has ability to address the creep curves of RAFM steel, for up to the onset of the tertiary regime. The advantage of the current approach is, it can predict the evolution of dislocation densities (mobile, dipole, and boundary), subgrain radius, dislocation glide velocity, climb velocity, internal stress, climb stress, effective stress, subgrain size, boundary pressure, boundary dislocation spacing, subgrain mobility, dipole capture spacing, softening due to precipitate and cavitation with ongoing creep. It is also possible to capture the change in each parameter with respect to each time step of the creep. The modeled creep curves are found to have a reasonable agreement with the experimental creep curves. Furthermore, other model outputs that are dislocation densities, precipitate and subgrain size are corroborated with the experimental data available in the literature [10, 49, 58, 159, 161-163, 173].

The following observation can be noted from the investigated conditions:

- Mobile and dipole dislocation density decrease with ongoing creep due to glide and climb recovery. Their predicted value at the end of numerical simulation lies in the range of 1.91 $\times 10^{13}$- 3.08 $\times 10^{14}$ m^{-2} and 1.27 $\times 10^{11}$ – 4.07 $\times 10^{12}$ m^{-2}, respectively.
- In the beginning of creep exposure, boundary dislocation density is found to be increasing and afterward decreases due to dominance of subgrain growth. It's predicted value after the completion of creep/numerical simulation lies in the range of 2.89-4.64 $\times 10^{14}$ m^{-2}.
- Radius of subgrain lies in the range of 0.308-0.458 µm at the end of the creep and it increases with ongoing creep.
- At the end of creep, the computed glide and climb velocities lie in the range 2.62 $\times 10^{-14}$-2.74 $\times 10^{-13}$ m/s and 3.41 $\times 10^{-15}$-3.53 $\times 10^{-14}$ m/s, respectively. The both dislocation velocities were found to be increasing with creep.
- The computed internal stress lies in the range of 4.96-20.20 MPa at the end of creep, for the explored conditions. It was observed that, the magnitude is decreasing with creep.
- The predicted magnitude of effective stress and boundary pressure is found to be in the range of 115-270 MPa and 2.06-3.58 MPa, respectively. The effective stress was observed to be increasing with creep. On the other hand, subgrain boundary pressure follows the trend of boundary dislocation density.
- At the end of numerical simulation, the carbides precipitate damage rate, carbonitrides precipitate damage rate and cavitation damage rate lies in the range 3.09 $\times 10^{-5}$ – 2.78 $\times 10^{-4}$ h^{-1}, 2.80 $\times 10^{-5}$ – 2.29 $\times 10^{-4}$ h^{-1} and 2.74 $\times 10^{-5}$ – 4.54 $\times 10^{-4}$ h^{-1}, respectively.
- Predicted boundary dislocation spacing decreases and subgrain boundary mobility increases with creep and lies in the range of 6.65-7.52 nm and 5.01 $\times 10^{-21}$-1.35 $\times 10^{-20}$ $mPa^{-1}s^{-1}$, respectively at the end of simulation.

- Predicted climb stress increases and dipole capture spacing decreases with creep and lies in the range of 17.16-25.8 MPa and 13-28 nm, respectively.

Appendix 4.A

Table 4.4. Model parameters utilized for the simulation of RAFM Steel

Parameters		In this work				Literature reported	Refs.
		500 ℃ / 280 MPa	600 ℃ / 140 MPa	550 ℃ / 200 MPa	600 ℃ / 120 MPa		
k_d	MX	45×10^{-47}	3×10^{-46}	9×10^{-47}	1×10^{-46}	2×10^{-42}	[52]
	$M_{23}C_6$	95×10^{-29}	5.7×10^{-28}	21×10^{-29}	16×10^{-29}	11×10^{-25}	[52]
a_1		0.32×10^{2}	0.57×10^{2}	0.04×10^{2}	0.41×10^{2}	$0.83\text{-}0.88\times10^{2}$	[57, 58, 200]
A		10.40×10^{2}	7.32×10^{2}	9.20×10^{2}	5.00×10^{2}	$7.65\text{-}10.5\times10^{2}$	[57, 58, 200]

Table 4.5. Material Constants utilized for the simulation of RAFM Steel

Constant	Value	Refs.
Shear Modulus, Pa (N/m^{-2})	$[91.65\text{-}0.015T+(2.645\times10^{-16})T^2-(190\times10^{-8})T^3]10^9$	[15]
Burgers vector, b(m)	2.866×10^{-10}	[55, 58]
Boltzmann constant, k_B	1.38×10^{-23}	[58]
Solute diffusion constant, D_s	1.38×10^{-20}	[201]
Annihilation distance, δ_{anh} (m)	3.00×10^{-9}	[55, 58]
Atomic volume, Ω (m^{-3})	2.35×10^{-29}	[55]
Dislocation interaction constant, α	0.02	[55]

Weight factor, c_{dip}	0.30	[55]
Taylor factor, M	3.00	[55, 57, 58]
Initial concentration of solute, C_0	0.06	[55]
Relative size misfit b/w solute and solvent, ε_a	0.08	[55]
ln(Inner outer cut off radius ratio)/ ln(r_2/r_1)	8.00	[154]